Nuclear Science and Techniques (2025) 36:237
https://doi.org/10.1007/s41365-025-01828-8

Asymmetric fission of ^{180}Hg and the role of hexadecapole moment

Yang Su[1] · Yong-Jing Chen[1] · Ze-Yu Li[1] · Li-Le Liu[1] · Guo-Xiang Dong[2] · Xiao-Bao Wang[2]

Received: 5 April 2025 / Revised: 7 June 2025 / Accepted: 19 June 2025 / Published online: 9 October 2025

Abstract
In this study, the fission properties of ^{180}Hg were investigated based on Skyrme density functional theory. The impact of the high-order hexadecapole moment (q_{40}) was observed at large deformations. With the q_{40} constraint, smooth and continuous potential energy surfaces could be obtained. In particular, the hexadecapole moment constraint is essential for obtaining appropriate scission configurations. The static fission path based on the PES supports the asymmetric fission of ^{180}Hg. The asymmetric distribution of the fission yields of ^{180}Hg was reproduced by the time-dependent generator coordinate method and agreed well with the experimental data.

Keywords Nuclear fission · Density functional theory · Hexadecapole moment · Potential energy surface · Mass distribution

1 Introduction

The asymmetric-fission mode in neutron-deficient ^{180}Hg was discovered in 2010 via β decay of ^{180}Tl [1]. For the fission of ^{180}Hg, its splitting into two ^{90}Zr fragments with magic $N = 50$ and semimagic $Z = 40$ is believed to dominate the fission process. However, unlike the initial theoretical prediction, ^{180}Hg has been observed to fission asymmetrically, with heavy and light fragment mass distributions centered around $A = 100$ and 80 nucleons, respectively, [1, 2].

Much theoretical research attention has been drawn to the puzzling fission behavior of ^{180}Hg. For example, macroscopic–microscopic models [1, 3–6] and self-consistent microscopic approaches [7–9] have been used to analyze multidimensional potential energy surfaces (PESs). The presence of an asymmetric saddle point with a rather high ridge between the symmetric and asymmetric-fission valleys is the main factor that determines the mass split in fission.

Calculations of fission fragment yields have also been performed for ^{180}Hg using the Brownian Metropolis shape motion treatment [3, 5, 10], Langevin equation [11], scission point model [4, 12–14], and random neck rupture mechanism [15], based on the PESs or scission configurations. The results are in approximate agreement with the experimental data, with a deviation of ~ four nucleons for the peak positions. Several attempts have also been made to describe the fragment mass distribution of ^{180}Hg in a fully microscopic manner, that is, the time-dependent generator coordinate method (TDGCM) based on covariant density functional theory (CDFT) [9]. The asymmetric peaks were reproduced very well, whereas a more asymmetric-fission mode with $A_H \sim 116$ was predicted, which was not observed in the experimental measurements.

In the theoretical study of nuclear fission, PES is an important infrastructure that describes the evolution of nuclear energy with its shape variations on its way from the initial configuration toward scission. In nuclear physics, there are generally two approaches to generating a PES. The first method is based on the historical liquid drop model [16–22] to the well-known macroscopic–microscopic model using parametrization of the nuclear mean-field deformation [23–33]. The other is based on microscopic self-consistent methods [34–43] or the constrained relativistic mean-field method [9, 44–50].

This work was supported by the National Key R and D Program of China (No. 2022YFA1602000), National Natural Science Foundation of China (Nos. 12275081 and U1732138), and Continuous-support Basic Scientific Research Project.

✉ Xiao-Bao Wang
xbwang@zjhu.edu.cn

[1] China Nuclear Data Center, China Institute of Atomic Energy, Beijing 102413, China

[2] School of Science, Huzhou University, Huzhou 313000, China

In the macroscopic–microscopic method, a predefined class of nuclear shapes is defined uniquely in terms of selecting appropriate collective coordinates, and a relatively smooth potential energy surface can be obtained. However, owing to limitations in computing resources, the microscopic calculation of the PES can only be performed within a limited number of deformation degrees of freedom. In the microscopic self-consistent method, higher-order collective degrees of freedom are incorporated self-consistently based on the variational principle. In fission studies, the quadrupole and octupole deformation (moments) constraints are natural and most often used to calculate microscopic PES.

However, several studies have shown that because of the absence of hexadecapole deformation (q_{40} or β_4), PES may exhibit discontinuities in large deformation scission regions [51–55]. Ref. [56] investigated the role of the hexadecapole deformation in the PES calculation of ^{240}Pu by applying a disturbance to β_4. The results show that one can obtain a smooth 2-dimensional PES in (β_2, β_3) by parallel calculations with a suitable disturbance of the hexadecapole deformation.

But for asymmetric fission of ^{180}Hg, there have been no reports about the effect of q_{40} or β_4 on the PES of ^{180}Hg. The self-consistent calculation in the quadrupole and octupole deformation spaces indicated that the PES of ^{180}Hg exhibits a different behavior from that of ^{240}Pu or ^{236}U with an increase in the quadrupole moment [7, 9]. Thus, it is interesting to examine the influence of the hexadecapole moment on the PES of ^{180}Hg under large deformations and analyze some properties of the scission configuration. In this study, we extend two-dimensional (q_{20}, q_{30}) constraint calculations to large deformation regions by adding q_{40} constraint to the microscopic PES calculation of ^{180}Hg. The importance of q_{40} in the self-consistent calculation of the PES for ^{180}Hg under large deformations was investigated. Moreover, the fission dynamics of ^{180}Hg, total kinetic energies, and fragment mass yield distributions based on TDGCM [57] are described and discussed.

2 Theoretical framework

To study the static fission properties, PES was determined using Skyrme density functional theory (DFT). The dynamic process was further investigated using the TDGCM framework. In this section, we briefly explain these two methods. A detailed description of Skyrme DFT can be found in Ref. [58], and the formulations of the TDGCM can be found in Refs. [57, 59–61].

2.1 Density functional theory

In the local density approximation of DFT, the total energy of finite nuclei can be calculated from the spatial integration of the Hamiltonian density $\mathcal{H}(\mathbf{r})$,

$$\mathcal{H}(\mathbf{r}) = \frac{\hbar^2}{2m}\tau(\mathbf{r}) + \sum_{t=0,1}\chi_t(\mathbf{r}) + \sum_{t=0,1}\breve{\chi}_t(\mathbf{r}). \tag{1}$$

In the above equation, $\tau(\mathbf{r})$, $\chi_t(\mathbf{r})$ and $\breve{\chi}_t(\mathbf{r})$ denote the densities of kinetic energy, potential energy, and pairing energy, respectively. The symbol $t = 0, 1$ denotes the isoscalar or isovector, respectively [62].

The mean-field potential energy $\chi_t(\mathbf{r})$ in the Skyrme DFT has the form generally as

$$\begin{aligned}\chi_t(\mathbf{r}) = {} & C_t^{\rho\rho}\rho_t^2 + C_t^{\rho\tau}\rho_t\tau_t + C_t^{J^2}\mathbb{J}_t^2 \\ & + C_t^{\rho\Delta\rho}\rho_t\Delta\rho_t + C_t^{\rho\nabla J}\rho_t\nabla\cdot\mathbf{J}_t,\end{aligned} \tag{2}$$

where the particle density ρ_t, kinetic density τ_t, and spin current vector densities $\mathbf{J}_t (t = 0, 1)$ can be calculated using the density matrix $\rho_t(\mathbf{r}\sigma, \mathbf{r}'\sigma')$, depending on the spatial ($\mathbf{r}$) and spin (σ) coordinates. In addition, $C_t^{\rho\rho}$, $C_t^{\rho\tau}$, etc. are coupling constants for different types of densities in the Hamiltonian density $\mathcal{H}(\mathbf{r})$, which are usually real numbers. As an exception, $C_t^{\rho\rho} = C_{t0}^{\rho\rho} + C_{tD}^{\rho\rho}\rho_0^{\gamma}$ is a density-dependent term. The formulations of the relation between the coupling constants and traditional Skyrme parameters can be found in Ref. [63]. For example, the spin–orbit force of the Skyrme interaction corresponds to term $C_t^{\rho\nabla J}\rho_t\nabla\cdot\mathbf{J}_t$.

The pairing correlation is often considered using the Hartree–Fock–Bogoliubov (HFB) approximation in DFT [58]. In the case of the Skyrme energy density functional, a commonly adopted pairing force is the density-dependent surface volume and zero-range potential, as given in Refs. [40, 64]:

$$\hat{V}_{\text{pair}}(\mathbf{r}, \mathbf{r}') = V_0^{(\text{n,p})}\left[1 - \frac{1}{2}\frac{\rho(\mathbf{r})}{\rho_0}\right]\delta(\mathbf{r} - \mathbf{r}'), \tag{3}$$

where $V_0^{(\text{n,p})}$ is the pairing strength for the neutron (n) and the proton (p), ρ_0 is the saturation density of nuclear matter fixed at 0.16 fm^{-3}, and $\rho(\mathbf{r})$ indicates the total density. As studied in Ref. [40], this type of pairing force is suitable for nuclear fission studies.

The DFT solver HFBTHO(V3.00) [65] was used to generate the PESs, in which axial symmetry was assumed; 26 major shells of the axial harmonic oscillator single-particle basis were used, and the number of basis states was further truncated to 1140. In this work, Skyrme DFT with SkM* parameters [66] is adopted, which is commonly used for fission studies. For the strength of pairing, $V_0^{(\text{n})} = -268.9$ MeV fm^3 and $V_0^{(\text{p})} = -332.5$ MeV fm^3 are used for the neutron and the proton, respectively, with the pairing window of $E_{\text{cut}} =$

60 MeV. This pairing strength, together with the choice of SkM* force and model space, has been adopted in Refs. [7, 67], in which a two-dimensional PES related to the fission of ^{180}Hg has been studied.

2.2 Time-dependent generator coordinate method

Nuclear fission is a large-amplitude collective motion that can be approximated as a slow adiabatic process driven by several collective degrees of freedom. In TDGCM, the many-body wave function of the fissioning system takes the generic form

$$|\Psi(t)\rangle = \int_{\mathbf{q}} f(\mathbf{q},t)|\Phi(\mathbf{q})\rangle \mathrm{d}\mathbf{q}, \tag{4}$$

where $|\Phi(\mathbf{q})\rangle$ is composed of known many-body wave functions with a vector of continuous variables $\mathbf{q}$. $\mathbf{q}$ are collections of variables chosen according to the physical problems.

For fission studies, two collective variables, quadrupole moment $\hat{q}_{20}$ and octupole moment $\hat{q}_{30}$, are usually adopted. In the above equation, the $f(\mathbf{q},t)$ is a weighted function. It is determined by the time-dependent Schrödinger-like equation, as

$$i\hbar\frac{\partial g(\mathbf{q},t)}{\partial t} = \hat{H}_{\mathrm{coll}}(\mathbf{q})g(\mathbf{q},t), \tag{5}$$

where the Gaussian overlap approximation (GOA) is used. $\hat{H}_{\mathrm{coll}}(\mathbf{q})$ is the collective Hamiltonian, as

$$\hat{H}_{\mathrm{coll}}(\mathbf{q}) = -\frac{\hbar^2}{2}\sum_{ij}\frac{\partial}{\partial q_i}B_{ij}(\mathbf{q})\frac{\partial}{\partial q_j} + V(\mathbf{q}), \tag{6}$$

in which $V(\mathbf{q})$ is the collective potential and $B_{ij}(\mathbf{q}) = \mathcal{M}^{-1}(\mathbf{q})$ is the inertia tensor as the inverse of the mass tensor $\mathcal{M}$. The potential and mass tensors were solved using the Skyrme DFT in this work. $g(\mathbf{q},t)$ contains information about the dynamics of the fissioning nuclei and is a complex collective wave function with collective variables $\mathbf{q}$.

To describe nuclear fission, the collective space is divided into an inner region and an external region for the nucleus to stay as a whole and the nucleus to separate into two fragments, respectively. The scission contour, which is a hypersurface, was used to separate these two regions. The flux of the probability current passing the scission contour can be used to evaluate the probability of observing two fission fragments at time t. For the surface element ξ on the scission contour, the integrated flux $F(\xi,t)$ is calculated by

$$F(\xi,t) = \int_{t=0}^{t}\mathrm{d}t\int_{\mathbf{q}\epsilon\xi}\mathbf{J}(\mathbf{q},t)\cdot\mathrm{d}\mathbf{S}, \tag{7}$$

as in Ref. [57], in which $\mathbf{J}(\mathbf{q},t)$ is the current

$$\mathbf{J}(\mathbf{q},t) = \frac{\hbar}{2i}B(\mathbf{q})[g^*(\mathbf{q},t)\nabla g(\mathbf{q},t) - g(\mathbf{q},t)\nabla g^*(\mathbf{q},t)]. \tag{8}$$

The yield of the fission product with the mass number A can be obtained by

$$Y(A) = C\sum_{\xi\epsilon\mathcal{A}}\lim_{t\to+\infty}F(\xi,t), \tag{9}$$

where $\mathcal{A}$ denotes an ensemble of all surface elements ξ on the scission contour containing the fragment with mass number A and C is the normalization factor to ensure that the total yield is normalized to 200. Similarly, the yield of fission fragments with charge number Z can also be obtained. In this study, the computer code FELIX(version 2.0) [61] was used to describe the time evolution of nuclear fission in the TDGCM-GOA framework.

3 Results and discussion

In the adiabatic approximation approach for fission dynamics, precise multidimensional PES is the first and essential step toward the dynamical description of fission. Figure 1 displays the PES contour of ^{180}Hg obtained by the HFB calculation in the collective space of (q_{20}, q_{30}), where q_{20} ranges from −20 b to 300 b and q_{30} ranges from 0 b$^{3/2}$ to 40 b$^{3/2}$ with a step of $\Delta q_{20} = 2$ b and $\Delta q_{30} = 2$ b$^{3/2}$. Overall, the PES pattern obtained in this work based on the DFT solver HFBTHO with the Skyrme SkM* functional is similar to that obtained using the symmetry unrestricted DFT solver HFODD [7] with the same functional and that obtained using covariant density functional theory with the relativistic PC-PK1 functional [9]. The static fission

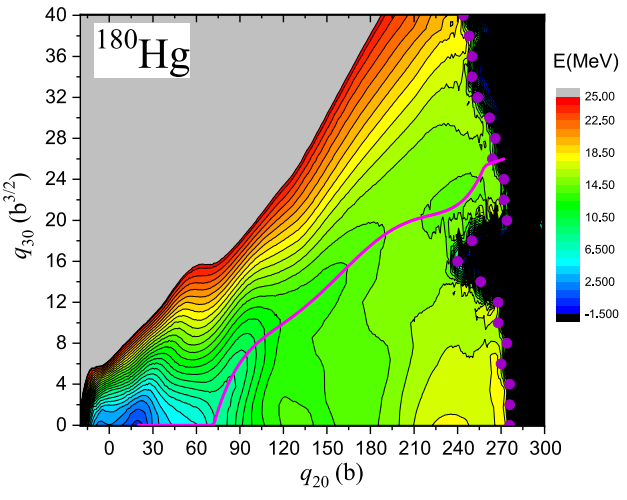

Fig. 1 (Color online) Potential energy surface of ^{180}Hg in the collective space of (q_{20}, q_{30}). The pink solid line and purple circle dots denote the static fission path and scission line, respectively

path starts from a nearly spherical ground state ($q_{20} = 20$ b, $q_{30} = 0$ b$^{3/2}$), the reflection-symmetric fission path can be found for small quadruple deformations, and the reflection-asymmetric path branches away from the symmetric path for $q_{20} = 100$ b. One can see that unlike the PES of actinide nuclei, there is no valley toward scission for ^{180}Hg, which undergoes a continuous uphill process until the mass asymmetric scission point with high q_{30} asymmetry.

In the (q_{20}, q_{30})-constrained PES calculations by DFT, other degrees of deformation are obtained based on the variational principle. In Refs. [55, 56], it has been learned that at a given q_{20} and q_{30}, there are two minima with different values of q_{40}, and the minimum with a larger q_{40} disappears when q_{20} is large enough, which indicates the transition toward scission. Hexadecapole deformation is an important degree of freedom for the description of PES under large deformations. In particular, a disturbance of the hexadecapole deformation is required for a smooth and reasonable PES, as shown in Ref. [56]. Thus, in our work, at large quadrupole moments, that is, larger than $q_{20} \simeq 200$ b ($\beta_2 \simeq 3.2$), a further constraint on the hexadecapole moment q_{40} is introduced. It is performed in a "perturbative" manner. A hexadecapole moment smaller than that obtained variationally is used as a further constraint in the first ten steps of DFT iterations, and it is then released to vary freely. Thus, a lower energy minimum with a smaller q_{40} can be obtained. This treatment was used to calculate the PES in Fig. 1 and is labeled "(B)" in Figs. 2 and 3. The calculation with the constraints q_{20} and q_{30} is labeled "(A)" in Figs. 2 and 3.

In Fig. 2, the energies of the static fission path as a function of quadruple moment q_{20} are shown. The symmetric ($q_{30} = 0$ b$^{3/2}$) and asymmetric-fission paths in ^{180}Hg are given, respectively. It can be clearly observed that these energies increase with q_{20} steadily. At approximately $q_{20} \sim 100$ b, the asymmetric-fission path starts to be favored in terms of energy compared to the symmetric fission path. The transitional valley that bridges the asymmetric and symmetric paths is shown in red in Fig. 2. Notably, this connection occurs at the deformation stage where the symmetric and asymmetric paths are nearly equivalent in energy. This characteristic of ^{180}Hg was verified in Ref. [68] using the HFB-Gogny D1S interaction. From Fig. 2, for case (A), one can see that the energy of ^{180}Hg increases continuously with q_{20}, and that it is difficult to rupture even at very large elongations, for example, $q_{20} \geq 300$ b ($\beta_{20} \geq 4.8$). As seen in case (B), with the inclusion of the q_{40} constraint, a gentle decent trend of energy occurs at $q_{20} \sim 240$ b, and a sudden drop in energy occurs at $q_{20} \sim 280$ b, indicating nuclear scission.

In Fig. 3, the hexadecapole moment (q_{40}), the average particle number around the neck (q_N), and the HFB energies are given as functions of q_{20}, respectively, at a given q_{30}. To investigate the role of q_{40}, only the region with large q_{20} is shown. From Fig. 3a, it can be seen that q_{40} increases nearly

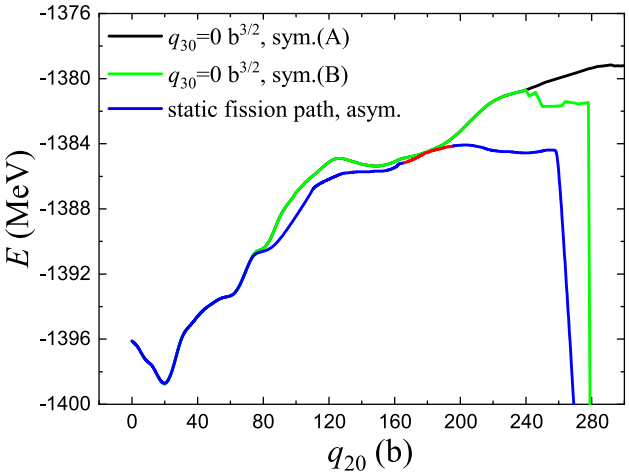

Fig. 2 (Color online) HFB energies along the symmetric-fission and asymmetric-fission pathways of ^{180}Hg as a function of q_{20}. The least-energy fission pathway (static fission path) is given as a blue curve. The symmetric-fission pathways are shown as the black or green curves, labeled as (A) or (B), respectively. These two curves are obtained with different treatment of q_{40} (see text for details). The red line shows the transitional valley that bridges the asymmetric and symmetric paths

linearly until a very large q_{20} value, especially for case (A), in which q_{40} can become very large during elongation. After a "perturbative" constraint on q_{40}, as the case (B) in the figure, the q_{40} value has sudden drop and then grow linearly. In studies of nuclear fission, q_N is often adopted as an indicator of nuclear scission. For example, $q_N = 4$ was used for the determination of the scission line of ^{240}Pu in Refs. [40, 54, 69]. In Fig. 3b, q_N gradually decreases with q_{20}. However, in case (A), the reduction in q_N becomes rather slow with an increase in q_{20}. In particular, at $q_{20} \sim 340$ b ($\beta_2 \sim 5.4$), $q_N > 4$ for $q_{30} = 0$ and 10 b$^{3/2}$, and the total energy increases continuously at a large q_{20}, as shown in Fig. 3c, respectively. After considering the q_{40} constraint, as shown in case (B) in Fig. 3b and c, both q_N and the total energy exhibit a sudden drop at approximately $q_{20} \sim 280$ b ($\beta_2 \sim 4.5$), indicating a nuclear rupture. It can be observed that when $q_N \leq 4$, q_N approaches zero with an increase in q_{20}.

To investigate the role of q_{40} on PES, the HFB energies and q_N against q_{40} at given q_{20} and q_{30} are plotted in Fig. 4, which were obtained through exact constrained calculations of q_{20}, q_{30} and q_{40}. In this figure, q_{30} is constrained to 0 b$^{3/2}$. The other q_{30} values were also tested, and the results were similar to those in Fig. 4. In Fig. 4a, one can see that there are two local minima along q_{40} degrees of freedom, which correspond to distinct valleys on the multidimensional potential energy surface. In Ref. [56], a similar trend in ^{240}Pu was found, and the minima related to the larger q_{40} disappeared with increasing quadruple deformation (at roughly $\beta_2 \sim 3.8$), leading to a natural transition to the minimum with

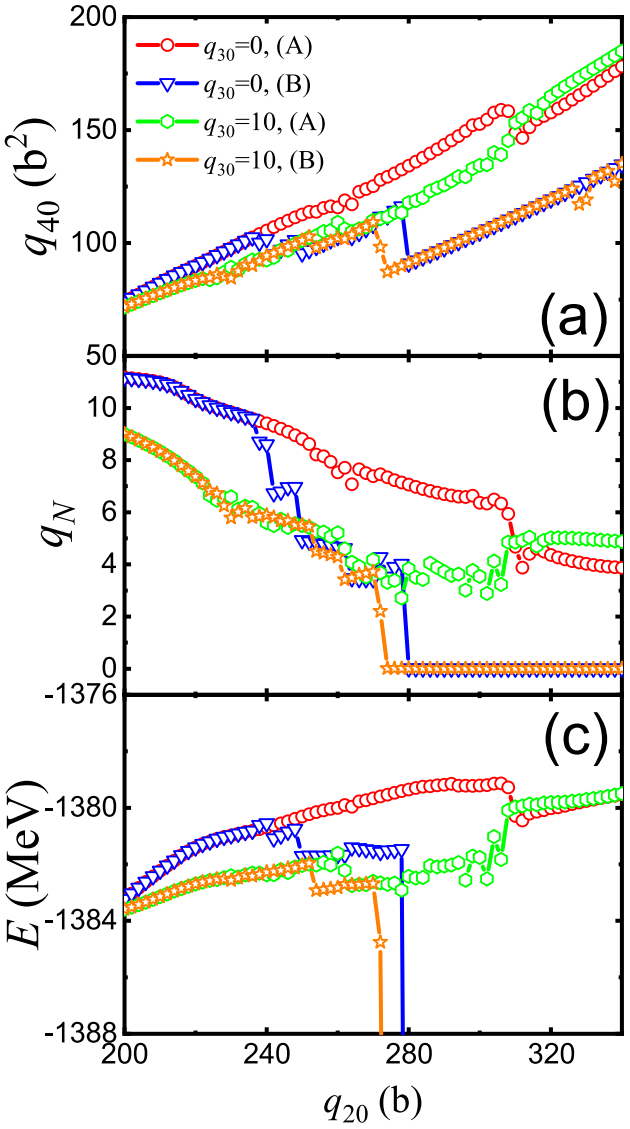

Fig. 3 (Color online) Hexadecapole moment (q_{40}), the particle number of neck (q_N), and HFB energies as a function of q_{20} are shown in panels (**a**), (**b**), and (**c**), respectively, for $q_{30} = 0$ b$^{3/2}$ and 10 b$^{3/2}$

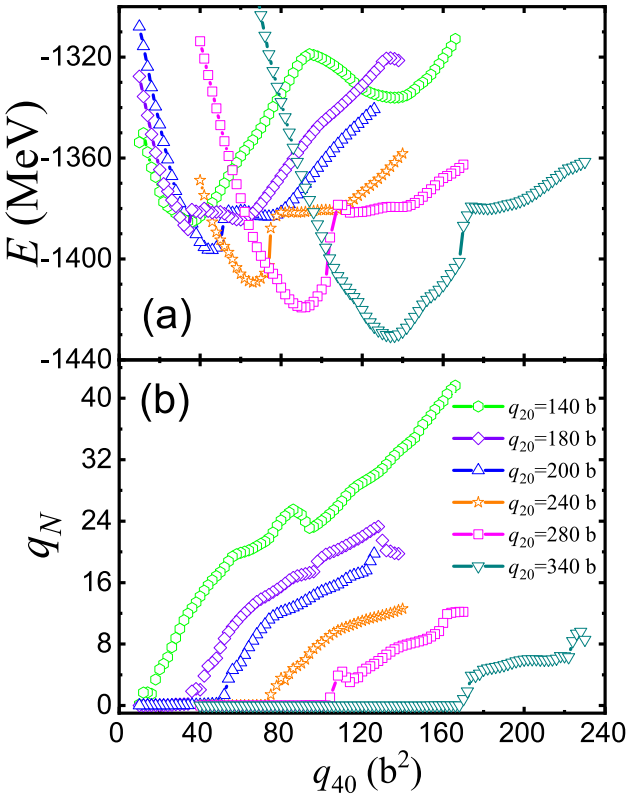

Fig. 4 (Color online) Panels **a** and **b** show HFB energies as functions of q_{20} under different treatments of the hexadecapole moment (q_{40}) for symmetric fission path ($q_{30} = 0$ b$^{3/2}$)

a smaller q_{40}. This transition causes the discontinuity and sudden drop in energy in the two-dimensional PES of (q_{20}, q_{30}). However, for ^{180}Hg, there remains an extremely soft and relatively flat minimum with larger q_{40} values, even at very large q_{20} values, for example, at $q_{20} = 340$ b ($\beta_2 \sim 5.4$). In the PES calculation with only the (q_{20}, q_{30}) constraint, q_{40} degrees of freedom are obtained by varying the total energies. As shown in Case (A) in Fig. 3, q_{40} after the variation calculation grows steadily, even at a very large q_{20}, and no transition to the minimum with a smaller q_{40} occurs. With only the (q_{20}, q_{30}) constraint, it is difficult to determine the proper scission configuration, at least for ^{180}Hg. After the "perturbative" inclusion of q_{40} constraint, as in case (B) in Fig. 3, such a transition can occur at large q_{20}. In Fig. 4b, it can be observed that q_N increases with q_{40}. q_N around the minimum with a larger q_{40} is approximately larger than 4, and when q_{20} >200 b, its value around the minimum with a smaller q_{40} is close to zero (numerically 10^{-3}–10^{-4}, effectively near zero). For $q_N \sim 0$, the nucleus is well separated into two fragments. From this calculation, one can learn that the introduction of q_{40} constraint in the self-consistent PES calculation can ensure the continuity of the potential energy surface. q_{40} is essential in DFT calculations for fission studies, particularly for the transition to scission.

Several results of the (q_{20}, q_{30}, q_{40}) constrained calculations are shown in Fig. 5 for the density distribution profiles of ^{180}Hg. q_{20} is constrained to 240 b, and q_{40} changes from 140 b^2 to 60 b^2 for $q_{30} = 0$ b$^{3/2}$ and $q_{30} = 10$ b$^{3/2}$ in the upper and lower panels, respectively. q_{40} degrees of freedom influenced the formation of neck and scission configurations. From the figure, it can be seen that, with a large q_{40}, there is no neck in the nucleus, and the nucleus is stretched very long. For the calculation with only the (q_{20}, q_{30}) constraint, as in case (A) in Figs. 2 and 3, q_{40} has a very large value with an increase in q_{20} and thus, the nucleus cannot undergo scission. With a decrease in q_{40}, the neck structure of the nucleus appears and becomes well separated when q_{40} has small values.

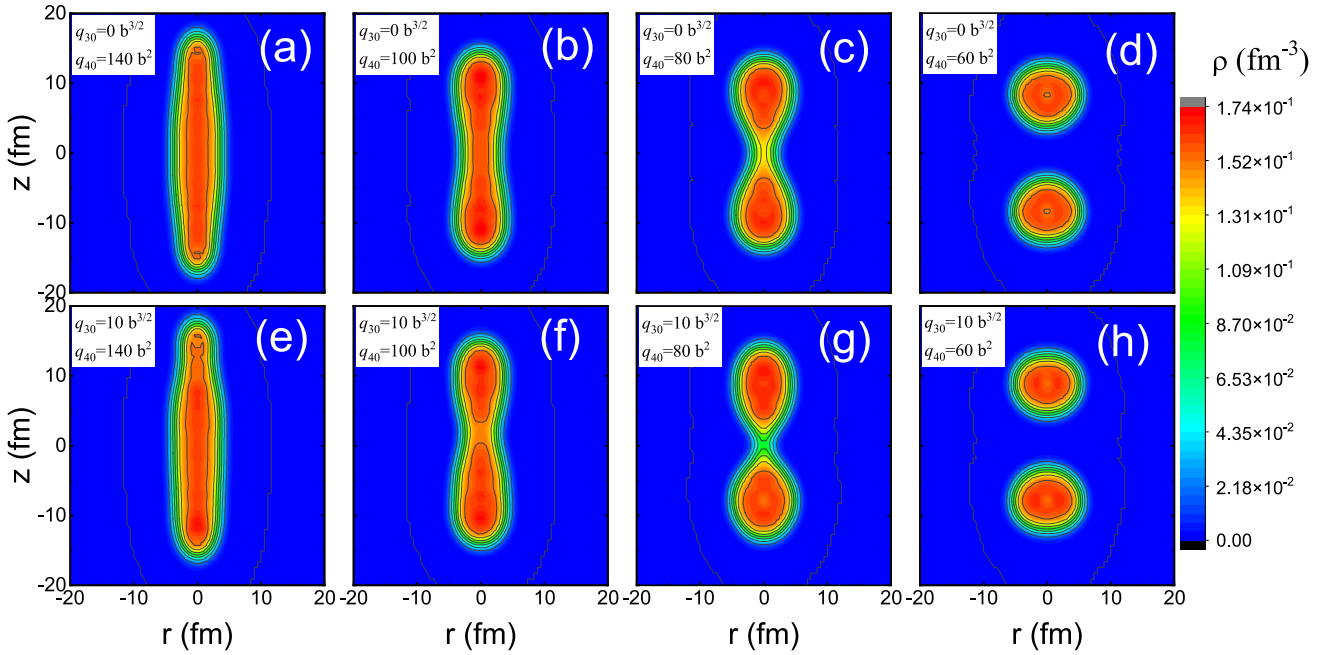

Fig. 5 (Color online) Density distributions of ^{180}Hg obtained with (q_{20}, q_{30}, q_{40}) constrained calculations. Results are obtained with different constrained q_{40} for symmetric fission channel (q_{20}, q_{30}) = (240 b, 0 b$^{3/2}$) (upper panels) and for asymmetric-fission channel (q_{20}, q_{30}) = (240 b, 10 b$^{3/2}$)(lower panels)

One of the most important quantities in induced fission is the total kinetic energy (TKE) carried out by the fission fragments. In this work, the total kinetic energy of the two separated fragments at scission point can be approximately estimated as the Coulomb repulsive interaction by using a simple formula $e^2Z_HZ_L/d_{ch}$, where e stands for the proton charge, Z_H and Z_L denote the charge numbers of the heavy and light fragments, respectively, and d_{ch} is the distance between the centers of charge of the two fragments at the scission point. Figure 6 displays the distribution of the calculated Coulomb repulsive energy based on the scission line indicated by the purple circle in Fig. 1 and compared it with the measured TKE [2]. It can be seen that the calculated results reproduce the trend of the measured TKE quite well, especially a dip at $A_H = 90$ and peak at $A_H = 94$, although the calculated results are generally overestimated about several MeV compared to data, which might be caused by the neglect of the dissipation effect.

Finally, we performed TDGCM+GOA calculations to model the time evolution of the fission dynamics of ^{180}Hg. Figure 7 shows the calculated mass distributions of the fission fragments of ^{180}Hg compared with the experimental data [1, 2]. The theoretical results in the framework of covariant density functional theory (CDFT) using PES generated with the neck coordinate constraint q_N from Ref. [9] are also given in the figure for comparison, denoted as "CDFT." As one of the most important microscopic inputs of fission dynamic calculations, the mass tensor was calculated using the GCM or ATDHFB methods in the present work. The calculated mass distribution is generally similar when using the mass tensor by these two methods, and better agreement was obtained by using the GCM method for the height of asymmetric peaks and symmetric valleys. Overall, the calculations accurately reproduced the experimental data. The calculated peak position deviated by one unit from the experimental peak position. The results of CDFT show

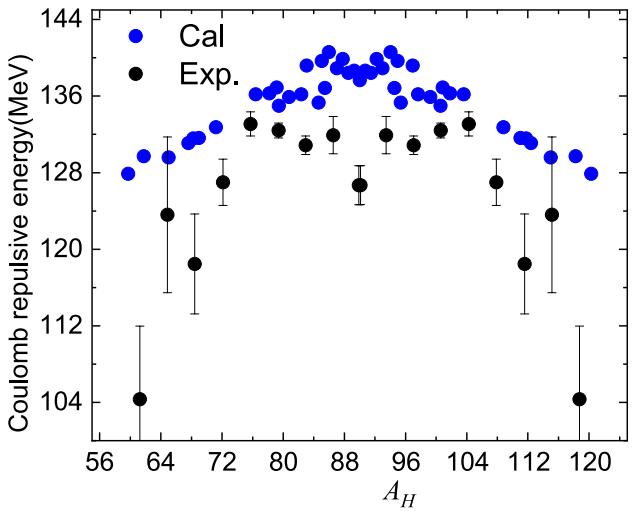

Fig. 6 (Color online) Calculated Coulomb repulsive energy of the nascent fission fragments for ^{180}Hg as functions of fragment mass, in comparison with the experimental data of the total kinetic energy [2]

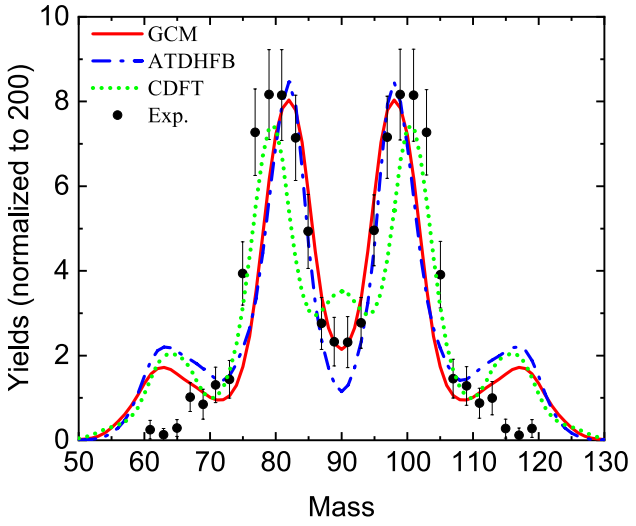

Fig. 7 (Color online) Mass distribution of the fission fragments of ^{180}Hg calculated by TDGCM method (lines), in comparison with the experimental data (circles) [1, 2]. The dash dot line and solid line stand for the calculation results with the ATDHFB mass tensor and GCM mass tensor, respectively. The dotted line is the calculation result in the framework of CDFT with PC-PK1 functional with q_N constraint from Ref. [9]

good asymmetric peak positions but overestimate the data and even predict a small peak for the symmetric valley. The deviation of the peak position from the data may have been caused by the mean-field potential. In the analysis of PES for ^{180}Hg in Ref. [7], it was found that the mass of the optimum fission fragment at the static scission point varies by two units when using either the Skyrme force or the Gogny force. In the dynamic calculation results, discrepancies were observed in the peak positions between the results based on Skyrme DFT and CDFT. The tail of fission fragment distribution is sensitive to the approximation of the mass tensor in dynamic calculations. The width of the distribution becomes slightly wider when the GCM mass tensor is used. Moreover, a more asymmetric-fission mode with $A_{\mathrm{H}} \sim 116$–117 was predicted in both this work and the CDFT calculation. As explained in Ref. [9], this mode resulted from the use of the initial state with mixed angular momenta, whereas in the experiment, there were only certain values owing to the selection rule of electron capture of ^{180}Tl. In the current study, these discrepancies from the data still exist as the initial state with mixed angular momenta.

4 Summary

In this study, the static fission properties and fission dynamics of ^{180}Hg were investigated using Skyrme DFT and TDGCM, respectively. During the calculation of the multidimensional PES, it was found that the hexadecapole moment is crucial for obtaining a smooth PES and proper scission configurations; thus, it is essential for fission dynamic studies. For the calculation of PES with only the q_{20} and q_{30} constraints, nuclear rupture does not occur, even at a very large q_{20}. Through calculations with q_{20}, q_{30}, and q_{40} constraints, it was found that a rather soft and flat minimum with a large hexadecapole moment still exists in the PES of ^{180}Hg even with a very elongated shape, which hinders the transition to the lower energy minimum with a smaller q_{40}. With the strategy of "perturbative" constraint of the collective freedom q_{40}, the transition to the minimum corresponding to the nuclear rupture could happen naturally, and thus, reasonable scission configurations can be obtained. From these scission configurations, the estimated distribution of the TKE reproduced the trend of the experimental data.

Based on the static PES calculation, the asymmetric-fission channel is favored in ^{180}Hg. Finally, the fission fragment yields were calculated using TDGCM. The calculated mass distributions also support asymmetric fission for ^{180}Hg. This calculation agrees well with the experimental data. Moreover, a more asymmetric peak with $A_{\mathrm{H}} \sim 117$ was predicted, which was also predicted by covariant DFT with the PC-PK1 parameter set [9].

Author contributions All authors contributed to the study conception and design. Material preparation, data collection, and analysis were performed by Yang Su, Yong-Jing Chen, Ze-Yu Li, Li-Le Liu, Guo-Xiang Dong, and Xiao-Bao Wang. The first draft of the manuscript was written by Yang Su, and all authors commented on previous versions of the manuscript. All authors read and approved the final manuscript.

Data availability The data that support the findings of this study are openly available in Science Data Bank at https://cstr.cn/31253.11.sciencedb.j00186.00861 and https://doi.org/10.57760/sciencedb.j00186.00861.

Declarations

Conflict of interest The authors declare that they have no Conflict of interest.

References

1. A.N. Andreyev, J. Elseviers, M. Huyse et al., New type of asymmetric fission in proton-rich nuclei. Phys. Rev. Lett. **105**, 252502 (2010). https://doi.org/10.1103/PhysRevLett.105.252502
2. J. Elseviers, A.N. Andreyev, M. Huyse et al., β-delayed fission of ^{180}Tl, Phys. Rev. C **88**, 044321 (2013); 102, 019908(E) (2020). https://doi.org/10.1103/PhysRevC.88.044321
3. T. Ichikawa, A. Iwamoto, P. Möller et al., Contrasting fission potential-energy structure of actinides and mercury isotopes. Phys. Rev. C **86**, 024610 (2012). https://doi.org/10.1103/PhysRevC.86.024610
4. A.V. Andreev, G.G. Adamian, N.V. Antonenko, Mass distributions for induced fission of different Hg isotopes. Phys. Rev. C **86**, 044315 (2012). https://doi.org/10.1103/PhysRevC.86.044315

5. P. Möller, J. Randrup, A.J. Sierk, Calculated fission yields of neutron-deficient mercury isotopes. Phys. Rev. C **85**, 024306 (2012). https://doi.org/10.1103/PhysRevC.85.024306
6. X. Guan, J. Guo, Q.W. Sun et al., On shape coexistence and possible shape isomers of nuclei around ^{172}Hg. Nucl. Sci. Tech. **36**, 128 (2025). https://doi.org/10.1007/s41365-025-01737-w
7. M. Warda, A. Staszczak, W. Nazarewicz, Fission modes of mercury isotopes. Phys. Rev. C **86**, 024601 (2012). https://doi.org/10.1103/PhysRevC.86.024601
8. J.. D. McDonnell, W. Nazarewicz, J.. A. Sheikh et al., Excitation-energy dependence of fission in the mercury region. Phys. Rev. C **90**, 021302(R) (2014). https://doi.org/10.1103/PhysRevC.90.021302
9. Z.Y. Li, S.Y. Chen, Y.J. Chen et al., Microscopic study on asymmetric fission dynamics of ^{180}Hg within covariant density functional theory. Phys. Rev. C **106**, 024307 (2022). https://doi.org/10.1103/PhysRevC.106.024307
10. P. Möller, J. Randrup, Calculated fission-fragment yield systematics in the region 74≤ Z ≤94 and 90≤ N ≤150. Phys. Rev. C **91**, 044316 (2015). https://doi.org/10.1103/PhysRevC.91.044316
11. V.L. Litnevsky, G.I. Kosenko, F.A. Ivanyuk et al., Description of the two-humped mass distribution of fission fragments of mercury isotopes on the basis of the multidimensional stochastic model. Phys. At. Nucl. **77**, 167 (2014). https://doi.org/10.1103/PhysRevC.91.044316
12. A.V. Andreev, G.G. Adamian, N.V. Antonenko et al., Isospin dependence of mass-distribution shape of fission fragments of hg isotopes. Phys. Rev. C **88**, 047604 (2013). https://doi.org/10.1103/PhysRevC.88.047604
13. S. Panebianco, J..-L. Sida, H. Goutte et al., Role of deformed shell effects on the mass asymmetry in nuclear fission of mercury isotopes. Phys. Rev. C **86**, 064601 (2012). https://doi.org/10.1103/PhysRevC.86.064601
14. D.Y. Huo, Z. Wei, K. Wu et al., Influence of octupole deformed shell structure on the asymmetric fission of mercury isotopes. Eur. Phys. J. A **60**, 244 (2024). https://doi.org/10.1140/epja/s10050-024-01456-7
15. M. Warda, A. Zdeb, Fission fragment mass yield deduced from density distribution in the pre-scission configuration. Phys. Scr. **90**, 114003 (2015). https://doi.org/10.1088/0031-8949/90/11/114003
16. L. Meitner, O.. R. Frisch, Disintegration of uranium by neutrons: a new type of nuclear reaction. Nature (London) **143**, 239 (1939). https://doi.org/10.1038/143239a0
17. N. Bohr, J.A. Wheeler, The mechanism of nuclear fission. Phys. Rev. **56**, 426 (1939). https://doi.org/10.1103/PhysRev.56.426
18. X. Dong-Ying Huo, C.H. Yang et al., Evaluation of pre-neutron-emission mass distributions of neutron-induced typical actinide fission using scission point model. Chin. Phys. C **45**, 114104 (2021). https://doi.org/10.1088/1674-1137/ac2298
19. F.L. Zou, X.J. Sun, K. Zhang et al., Pre-neutron fragment mass yields for ^{235}U(n, f) and ^{239}Pu(n, f) reactions at incident energies from thermal up to 20 MeV. Chin. Phys. C **47**, 044101 (2023). https://doi.org/10.1088/1674-1137/acb910
20. Y.N. Han, Z. Wei, Y.X. Wang et al., Calculation of the energy dependence of fission fragments yields and kinetic energy distributions for neutron-induced ^{235}U fission. Chin. Phys. C **48**, 084102 (2024). https://doi.org/10.1088/1674-1137/ad485c
21. Q.F. Song, L. Zhu, H. Guo et al., Verification of neutron-induced fission product yields evaluated by a tensor decompsition model in transport-burnup simulations. Nucl. Sci. Tech. **34**, 32 (2023). https://doi.org/10.1007/s41365-023-01176-5
22. Z.X. Fang, M. Yu, Y.G. Huang et al., Theoretical analysis of long-lived radioactive waste in pressurized water reactor. Nucl. Sci. Tech. **32**, 72 (2021). https://doi.org/10.1007/s41365-021-00911-0
23. P. Möller, D.G. Madland, A.J. Sierk, Nuclear fission modes and fragment mass asymmetries in a five-dimensional deformation space. Nature (London) **409**, 785 (2001). https://doi.org/10.1038/35057204
24. Yu.V. Pyatkov, V.V. Pashkevich, A.V. Unzhakova et al., Manifestation of clustering in the ^{252}Cf(sf) and ^{249}Cf(n_{th}, f) reactions. Nuclear Phys. A **624**, 140 (1997). https://doi.org/10.1016/S0375-9474(97)00417-X
25. K. Pomorski, B. Nerlo-Pomorska, J. Bartel et al., Stability of superheavy nuclei. Phys. Rev. C **97**, 034319 (2018). https://doi.org/10.1103/PhysRevC.97.034319
26. K. Pomorski, A. Dobrowolski, R. Han et al., Mass yields of fission fragments of Pt to Ra isotopes. Phys. Rev. C **101**, 064602 (2020). https://doi.org/10.1103/PhysRevC.101.064602
27. X. Guan, J.H. Zheng, M.Y. Zheng, Pairing effects on the fragment mass distribution of Th, U, Pu, and Cm isotopes. Nucl. Sci. Tech. **34**, 173 (2023). https://doi.org/10.1007/s41365-023-01316-x
28. L.L. Liu, X.Z. Wu, Y.J. Chen et al., Study of fission dynamics with a three-dimensional Langevin approach. Phys. Rev. C **99**, 044614 (2019). https://doi.org/10.1103/PhysRevC.99.044614
29. L.L. Liu, Y.J. Chen, X.Z. Wu et al., Analysis of nuclear fission properties with the Langevin approach in Fourier shape parametrization. Phys. Rev. C **103**, 044601 (2021). https://doi.org/10.1103/PhysRevC.103.044601
30. L.L. Liu, X.Z. Wu, Y.J. Chen et al., Influence of the neck parameter on the fission dynamics within the two-center shell model parametrization. Chin. Phys. C **46**, 124101 (2022). https://doi.org/10.1088/1674-1137/ac8867
31. Y. Su, Z.Y. Li, L.L. Liu et al., Calculation of fission potential energy surface and fragment mass distribution based on Fourier nuclear shape parametrization. Atomic Energy Sci. Technol. **55**, 2290–2299 (2021). https://doi.org/10.7538/yzk.2021.youxian.0614. (**in Chinese**)
32. L.L. Liu, Y.J. Chen, Z.G. Ge et al., Energy dependence of fission product yields in ^{235}U(n, f) within the Langevin approach incorporated with the statistical model. Chin. Phys. C **49**, 054112 (2025). https://doi.org/10.1088/1674-1137/adb70b
33. X. Guan, W.Q. Jiang, T.C. Wang et al., Fission barriers of actinide isotopes in the exactly solvable pairing model. Nucl. Phys. Rev. **40**, 502 (2023). https://doi.org/10.11804/NuclPhysRev.40.2023013
34. M. Warda, J.L. Egido, L.M. Robledo et al., Self-consistent calculations of fission barriers in the Fm region. Phys. Rev. C **66**, 014310 (2002). https://doi.org/10.1103/PhysRevC.66.014310
35. T.R. Rodriguez, J.L. Egido, Triaxial angular momentum projection and configuration mixing calculations with the Gogny force. Phys. Rev. C **81**, 064323 (2010). https://doi.org/10.1103/PhysRevC.81.064323
36. N. Hinohara, T. Nakatsukasa, M. Matsuo et al., Microscopic description of oblate-prolate shape mixing in proton-rich Se isotopes. Phys. Rev. C **80**, 014305 (2009). https://doi.org/10.1103/PhysRevC.80.014305
37. L. Bonneau, Fission modes of ^{256}Fm and ^{258}Fm in a microscopic approach. Phys. Rev. C **74**, 014301 (2006). https://doi.org/10.1103/PhysRevC.74.014301
38. Y.J. Chen, Y. Su, G.X. Dong et al., Energy density functional analysis of the fission properties of ^{240}Pu: the effect of pairing correlations. Chin. Phys. C **46**, 024103 (2022). https://doi.org/10.1088/1674-1137/ac347a
39. Y.J. Chen, Y. Su, L.L. Liu et al., Microscopic study of neutron-induced fission process of ^{239}Pu via zero- and finite-temperature density functional theory. Chin. Phys. C **47**, 054103 (2023). https://doi.org/10.1088/1674-1137/acbe2c
40. Su. Yang, Ze.-Yu. Li, Li.-Le. Liu et al., Sensitivity impacts owing to the variations in the type of zero range pairing forces on the

fssion properties using the density functional theory. Nucl. Sci. Tech. **35**, 62 (2024). https://doi.org/10.1007/s41365-024-01422-4
41. Y. Qiang, J.C. Pei, Energy and pairing dependence of dissipation in real-time fission dynamics. Phys. Rev. C **104**, 054604 (2021). https://doi.org/10.1103/PhysRevC.104.054604
42. Y. Qiang, J.C. Pei, P.D. Stevenson, Fission dynamics of compound nuclei: pairing versus fluctuations. Phys. Rev. C **104**, L031304 (2021). https://doi.org/10.1103/PhysRevC.103.L031304
43. Y. Su, Z.Y. Li, L.L. Liu et al., Investigation of the impact of pairing correlations on the nuclear fission process based on the energy density functional theory. Nucl. Phys. Rev **41**, 127 (2024). https://doi.org/10.11804/NuclPhysRev.41.2023CNPC84
44. Z.X. Ren, J. Zhao, D. Vretenar et al., Microscopic analysis of induced nuclear fission dynamics. Phys. Rev. C **105**, 044313 (2022). https://doi.org/10.1103/PhysRevC.105.044313
45. B. Li, D. Vretenar, Z.X. Ren et al., Fission dynamics, dissipation, and clustering at finite temperature. Phys. Rev. C **107**, 014304 (2023). https://doi.org/10.1103/PhysRevC.107.014303
46. B. Li, D. Vretenar, Z.X. Ren et al., Time-dependent density functional theory study of induced-fission dynamics of ^{226}Th. Phys. Rev. C **110**, 034302 (2024). https://doi.org/10.1103/PhysRevC.110.034302
47. J.-Y. Guo, P. Jiao, X.-Z. Fang, Microscopic description of nuclear shape evolution from spherical to octupole-deformed shapes in relativistic mean-field theory. Phys. Rev. C **82**, 047301 (2010). https://doi.org/10.1103/PhysRevC.82.047301
48. H. Tao, J. Zhao, Z.P. Li et al., Microscopic study of induced fission dynamics of ^{226}Th with covariant energy density functionals. Phys. Rev. C **96**, 024319 (2017). https://doi.org/10.1103/PhysRevC.96.024319
49. M.H. Zhou, Z.Y. Li, S.Y. Chen et al., Three-dimensional potential energy surface for fission of ^{236}U within covariant density functional theory. Chin. Phys. C **47**, 064106 (2023). https://doi.org/10.1088/1674-1137/acc4ac
50. J. Zhao, T. Nikšić, D. Vretenar, Microscopic self-consistent description of induced fission: dynamical pairing degree of freedom. Phys. Rev. C **104**, 044612 (2021). https://doi.org/10.1103/PhysRevC.104.044612
51. A. Zdeb, M. Warda, L.M. Robledo, Description of the multidimensional potential-energy surface in fission of ^{252}Cf and ^{258}No. Phys. Rev. C **104**, 014610 (2021). https://doi.org/10.1103/PhysRevC.104.014610
52. N. Dubray, D. Regnier, Numerical search of discontinuities in self-consistent potential energy surfaces. Comput. Phys. Commun. **183**, 2035 (2012). https://doi.org/10.1016/j.cpc.2012.05.001
53. D. Regnier, N. Dubray, N. Schunck, From asymmetric to symmetric fission in the fermium isotopes within the time-dependent generator-coordinate-method formalism. Phys. Rev. C **99**, 024611 (2019). https://doi.org/10.1103/PhysRevC.99.024611
54. N. Schunck, D. Duke, H. Carr et al., Description of induced nuclear fission with Skyrme energy functionals: static potential energy surfaces and fission fragment properties. Phys. Rev. C **90**, 054305 (2014). https://doi.org/10.1103/PhysRevC.90.054305
55. J.F. Berger, M. Girod, D. Gogny, Microscopic analysis of collective dynamics in low energy fission. Nucl. Phys. A **428**, 23 (1984). https://doi.org/10.1016/0375-9474(84)90240-9
56. J.H. Chi, Y. Qiang, C.Y. Gao et al., Role of hexadecapole deformation in fission potential energy surfaces of ^{240}Pu. Nucl. Phys. A **1032**, 122626 (2023). https://doi.org/10.1016/j.nuclphysa.2023.122626
57. D. Regnier, N. Dubray, N. Schunck et al., Fission fragment charge and mass distributions in ^{239}Pu(n, f) in the adiabatic nuclear energy density functional theory. Phys. Rev. C **93**, 054611 (2016). https://doi.org/10.1103/PhysRevC.93.054611
58. M. Bender, P.H. Heenen, P.G. Reinhard, Self-consistent mean-field models for nuclear structure. Rev. Mod. Phys. **75**, 121 (2003). https://doi.org/10.1103/RevModPhys.75.121
59. J.F. Berger, M. Girod, D. Gogny, Time-dependent quantum collective dynamics applied to nuclear fission. Comput. Phys. Commun. **63**, 365 (1991). https://doi.org/10.1016/0010-4655(91)90263-K
60. R. Bernard, H. Goutte, D. Gogny et al., Microscopic and nonadiabatic Schrödinger equation derived from the generator coordinate method based on zero- and two-quasiparticle states. Phys. Rev. C **84**, 044308 (2011). https://doi.org/10.1103/PhysRevC.84.044308
61. D. Regnier, N. Dubray, M. Verriere et al., FELIX-2.0: new version of the finite element solver for the time dependent generator coordinate method with the Gaussian overlap approximation. Comput. Phys. Commun. **225**, 180 (2018). https://doi.org/10.1016/j.cpc.2017.12.00
62. E. Perlińska, S.G. Rohoziński, J. Dobaczewski et al., Local density approximation for proton-neutron pairing correlations: formalism. Phys. Rev. C **69**, 014316 (2004). https://doi.org/10.1103/PhysRevC.69.014316
63. J. Dobaczewski, J. Dudek, Time-odd components in the mean-field of rotating superdeformed nuclei. Phys. Rev. C **52**, 1827 (1995). https://doi.org/10.1103/PhysRevC.52.1827
64. N. Schunck, L.M. Robledo, Microscopic theory of nuclear fission: a review. Rep. Prog. Phys. **79**, 116301 (2016). https://doi.org/10.1088/0034-4885/79/11/116301
65. R. Navarro Perez, N. Schunck, R.D. Lasseri et al., Axially deformed solution of the Skyrme-Hartree-Fock-Bogolyubov equations using the transformed harmonic oscillator basis (III) HFBTJO (v3.00): A new version of the program. Comput. Phys. Commun. **220**, 363 (2017). https://doi.org/10.1016/j.cpc.2017.06.022
66. J. Bartel, P. Quentin, M. Brack et al., Towards a better parametrisation of Skyrme-like effective forces: A critical study of the SkM force. Nucl. Phys. A **386**, 79 (1982). https://doi.org/10.1016/0375-9474(82)90403-1
67. M. Warda, A. Staszczak, L. Próchniak, Comparison of self-consistent Skyrme and Gogny calculations for light Hg isotopes. Int. J. Mod. Phys. E **19**, 787 (2010). https://doi.org/10.1142/S0218301310015230
68. R.N. Bernard, C. Simenel, G. Blanchon et al., Fission of ^{180}Hg and ^{264}Fm: a comparative study. Eur. Phys. J. A **60**, 192 (2024). https://doi.org/10.1140/epja/s10050-024-01415-2
69. X.B. Wang, Y.J. Chen, G.X. Dong et al., Role of pairing correlations in the fission process. Phys. Rev. C **108**, 034306 (2023). https://doi.org/10.1103/PhysRevC.108.034306